Chapter 19

Thermal and linear-elastic properties of lightweight concrete

Amaury Vannier-Moreau, François Willot & Dominique Jeulin

Mines ParisTech, PSL – Research University, Centre for Mathematical Morphology, 35 rue Saint-Honoré, 77300 Fontainebleau, France

Keywords: Fourier methods; Lightweight concrete; Segmentation

Abstract This work is concerned by the prediction of the linear-elastic and thermal properties of lightweight agregate concrete. The 3D microstructures of two samples, with low and high-porosity, are imaged using microtomography. Image analysis techniques are used to segment the pores in each microstructure. First, Fourier-based computations are carried out to determine the elastic macroscopic response, using experimental data for the elastic moduli of the cement paste. These results are compared with experimental measurements of the elastic response of the samples. Numerical and experimental results are compared and discussed. Second, the thermal response is considered. We determine, using Fourier methods, the thermal conductivity of the matrix that allows one to recover the experimental data for the effective thermal response of the samples. We highlight how the apparent discrepancies between Fourier-based computations and experimental data might be resolved.

19.1 Lightweight concrete with entrained air

Lightweight concrete are a family of concrete materials with density lower than 2000 $\mathrm{kg\,m^{-3}}$. These materials, which contain a high volume of entrained air, exhibit very good acoustic shielding and thermal insulating properties (see e.g. (Kim, Jeon, and Lee 2012)). The present work centers around two samples of cellular-type lightweight concrete, denoted "Bul 55" and "Bul 61", with a volumetric mass of 1040 and 1410 $\mathrm{kg\,m^{-3}}$, respectively, when dry. The two samples were provided by the Centre d'études et de recherches de l'industrie du béton (CERIB) in France. Microtomography images in 3D have been obtained by A. Fanget at CEA, Gramat (Fig. 19.1). Their resolution is 3.23 µm per voxel for the Bul 55 sample and 3.34 for the Bul 61 sample. The two concrete samples are made from a cement paste, with different forming process, resulting in different pore sizes and porosity. The largest pore is about 300 µm for Bul 55 and 150 µm for Bul 61. The image size is $4000\times\ 4000\times\ 1400$ for the two acquisitions. The largest rectangular parallelepiped fully enclosed in each concrete sample is about $16000\times\ 16000\times\ 1100$. In the folowing, all morphological treatments are carried out on a cuboid of size 1024^3 voxels extracted from the center region of the 3D images.

The experimental data provided by the CERIB include the volumetric porosity of the two samples, their effective thermal conductivity at 10°C, Young modulus and Poisson

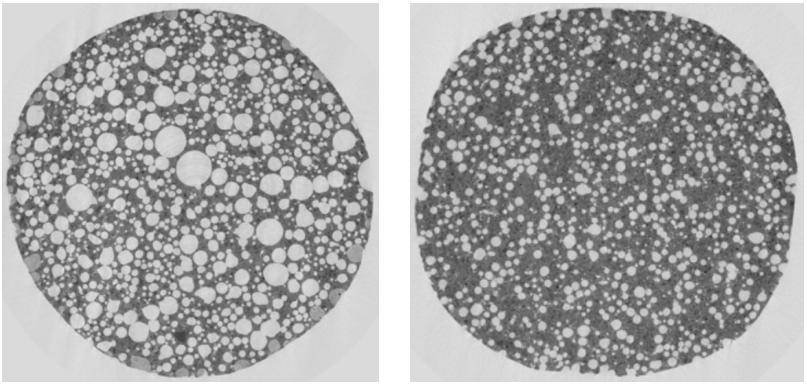

(a) (b)

Figure 19.1: 3D microtomography images of lightweight concrete samples "Bul 55" (a) and "Bul 61" (b). Number of voxels: 4000× 4000× 1400. Images: A. Fanget.

Sample	porosity	λ (W/m/K)	E (GPa)	ν
Bul 55	50%	0.331	11.0	0.18
Bul 61	33%	0.470	13.5	0.12

Table 19.1: Porosity, macroscopic thermal conductivity λ, Young Modulus E and Poisson ratio ν for lightweighted concrete samples Bul 55 and Bul 61, determined experimentally.

ratio (Tab. 19.1). Furthermore, CERIB indicates that the same cement paste has been used for both concrete samples. Experimental measurement carried out on the cement paste (in the absence of macroscopic pores) gives a Young modulus of 25.9 GPa. CERIB also gives an (indicative) Poisson coefficient of about 0.2 for the cement paste.

19.2 3D segmentation

The microtomography images are well contrasted. Nevertheless, parasital glinces are observed in the sement paste, and small pores frontiers are sometimes blurred (Fig. 19.1). The images can not be directly thresholded, and are accordingly segmented in three steps, illustrated in Fig. 19.2, where a 2D cut of a small cube inside the volume is shown. First, an alternate sequential filter of size 1 is computed (results shown in maps 19.2a and 19.2d). Second, the material are segmented into two phases, using the method in (Otsu 1979). The resulting images contain fictitious pores, of small size, that are really noise in the microtomography images (maps 19.2b and 19.2e). The later are removed in a third step using an morphological opening of volume 170 voxels (equivalent to a sphere of diameter 7 voxels). We then remove part of the cement paste entirely contained in air (maps 19.2c and 19.2f). The porosity measured on the segmented images is 51% for the Bul 55 sample and 27% for Bul 61. The former value is very close to that reported experimentally (Tab. 19.1) whereas the later is underestimated by 6% in the segmented image. This suggests the presence of microporosity in Bul 61's cement paste not visible in the microtomography image.

The granulometry of the pores are determined numerically for each sample using morphological closing of increasing size (Fig. 19.3). The curves indicate the presence, in sample Bul 61, of at least two distinct populations of pores, one of size less than about 50 µm, and the other of size between about 50 and 150 µm. Sample Bul 55 contains much larger pores, of size up to 320 µm.

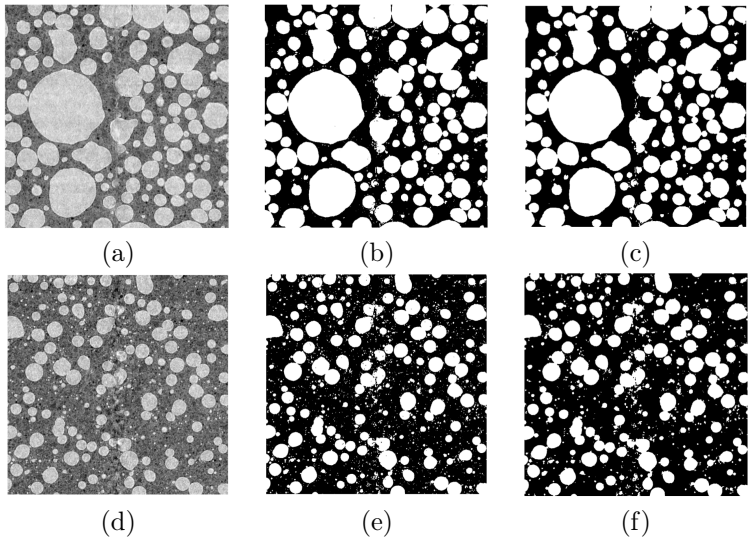

Figure 19.2: Main steps of 3D image segmentation (2D detail) for samples "Bul 55" (a,b,c) and "Bul 61" (d,e,f): after filtering (a,d); after thresholding (b,e) and after correction of the binary image (c,f).

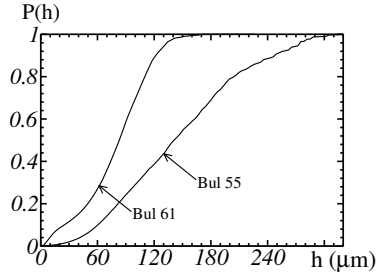

Figure 19.3: Granulometry curve, represented as a cumulative distribution $P(h)$, of the pores in samples Bul 55 and Bul 61. $P(h)$ is the probability in number that a pore size is less than h, where the pore size is defined by a morphological closing.

19.3 FFT results vs. experimental data

19.3.1 Elastic response

We carry out FFT computations on the central parts of the segmented images of size 1024^3 voxels, using the augmented Lagrangian Fourier method in (Michel, Moulinec, and Suquet 2000). Strain loadings are applied in the six directions. Maps of various stress components are shown in Fig. (19.4) for two applied strain loadings, hydrostatic and shear. An isotropic macroscopic response is recovered for the effective tensor $\widetilde{\mathbf{C}}$, up to two or three percent variations. For instance, for Bul 55, we obtain $\widetilde{C}_{1111} = 6.55 \approx \widetilde{C}_{2222} = 6.28$.

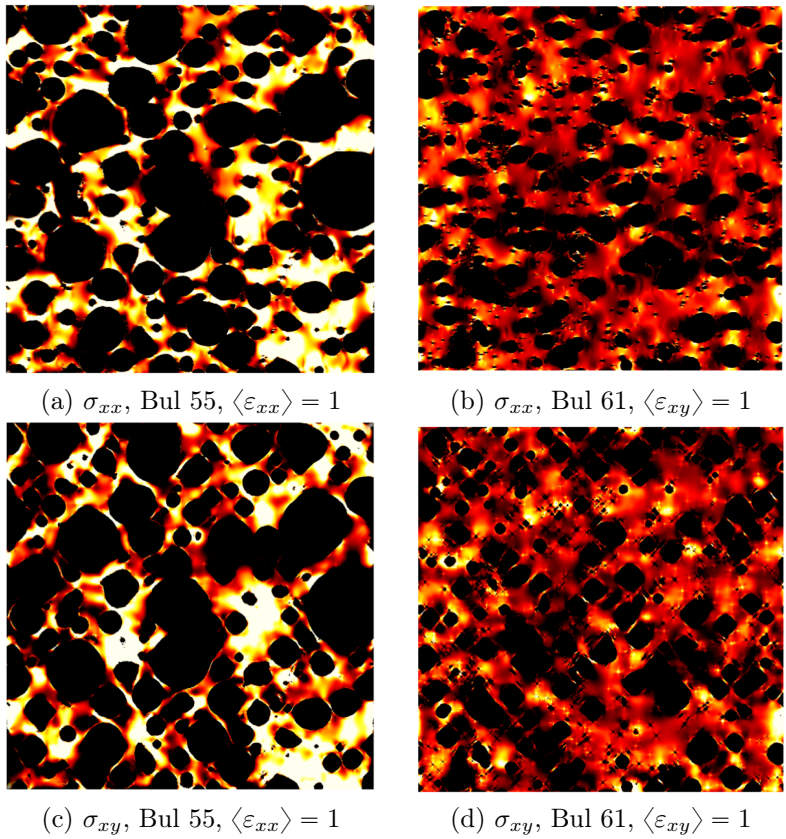

(a) σ_{xx}, Bul 55, $\langle \varepsilon_{xx} \rangle = 1$ (b) σ_{xx}, Bul 61, $\langle \varepsilon_{xy} \rangle = 1$

(c) σ_{xy}, Bul 55, $\langle \varepsilon_{xx} \rangle = 1$ (d) σ_{xy}, Bul 61, $\langle \varepsilon_{xy} \rangle = 1$

Figure 19.4: FFT maps of the traction component σ_{xx} (a,b) and shear component σ_{xx} (c,d) along a 2D plane parallel to the x and y axis: with mean applied strain $\langle \varepsilon_{xx} \rangle = 100\%$ (a,b) and $\langle \varepsilon_{xy} \rangle = 100\%$ (c,d) for samples Bul 55 (a,c) and Bul 61 (b,d). The stress field is zero in the black regions. Highest stress values (different in each map) in white.

The effective Young moduli predicted by Fourier computations are given in Tab. (19.2). The Young modulus predicted for sample Bul 61 is in good agreement with experimental data, with 10% relative difference between the two. This is not the case for Bul 55, which is 45% more compliant according to Fourier results than in reality. As expected, the upper-bound for the Young modulus (column 4, Tab. 19.2), computed from the Hashin-Shtrikman's (HS) upper-bound, is stiffer than the FFT predictions. However, experimental data from sample Bul 55 violates the bound ($E \approx 11$ GPa, $> E^{\text{HS}} = 8.3$).

This difference can not be explained solely by the effect of the Poisson ratio in the cement paste. For instance, the Hashin and Shtrikman's upper-bound for the Young

Sample	E^{FFT} (GPa)	ν^{FFT}	E^{HS} (GPa)	ν^{HS}
Bul 55	5.6	0.17	8.3	0.17
Bul 61	12.2	0.17	16.0	0.17

Table 19.2: Effective Young modulus E and Poisson ratio ν for lightweighted concrete samples Bul 55 and Bul 61, predicted numerically and analytically, using the Hashin and Shtrikman bounds.

modulus of sample Bul 55 varies between 8.3 and 8.6 when the Poisson ratio in the matrix takes on values in the range $0 \leqslant \nu \leqslant 0.47$. Likewise, the Young modulus is quite insensitive to the Poisson ratio, when one considers the Hashin-Shtrikman bounds relevant to sample Bul 61, with porosity 33%. To explain the difference between FFT predictions and experimental results for the Young modulus of sample Bul 55, one has to assume that the Young modulus in the cement paste is roughly 33% stiffer than experimental measurements, i.e. equal to about 38 GPa, instead of 29 GPa.

The presence of micro-cracks or micro-porosity in the cement paste of sample Bul 61 could potentially explain such difference. In this scenario, the cement paste of Bul 61 contains, contrary to sample Bul 55, micronic or sub-micronic micro-cracks or micro-porosity. These cracks or pores are not resolved in the microtomography image of Bul 61, as suggested by the granulometry curves (Fig. 19.3). Assume also that the experimental measurement are made on a *damaged* cement paste containing micro-cracks and porosity. The undamaged cement paste must then have Young modulus equal to about 51 GPa and Poisson ratio 0.17. With these values, one recovers the experimental Young modulus for sample Bul 55 predicted by FFT. The effective modulus is indeed about $51/25.9 \times 5.6 = 11$ GPa, neglecting Poisson ratio effect. Cracks or sub-micronic pores are present in the cement paste of sample Bul 61, which explains the measured Young modulus of 26 GPa and the experimental Young modulus for Bul 61.

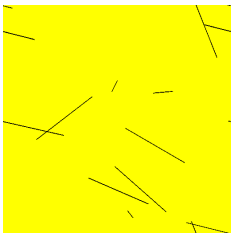

Figure 19.5: Boolean model of disks with density $\eta = 0.23$. 2D cut of a 3D microstructure.

Clearly, the presence of 6% of micro-porosity in the cement paste of sample Bul-61 is insufficient to explain such a difference alone: using HS bounds again, such porosity would lower the Young modulus from 51 to 44 GPa. Micro-cracks however, have a strong effect on the macroscopic Young moduli. This effect can be quantified by e.g. the self-consistent estimate in (Willot, Trumel, and Jeulin 2018). According to this analytical estimate, the value of 26 GPa for the damaged cement paste is recovered provided the cement paste contains 6% microporosity and a density of cracks $\eta \approx 0.23$. The adimensional density of cracks is defined, for a set of equi-sized disk of radius a, by $\eta = na^3/V$ where n is the number of cracks in the volume V, see (Bristow 1960). A 2D section of a 3D Boolean model of disks with this density is shown in Fig. (19.5) for illustration. This hypothesis can not be confirmed without higher-resolution images. Nevertheless, we have observed the presence of at least three micro-cracks in the microtomography image for Bul 61 (see Fig. 19.6), suggesting the presence of cracks at lower length scales. No such crack has been observed in the microtomography image of sample Bul 55.

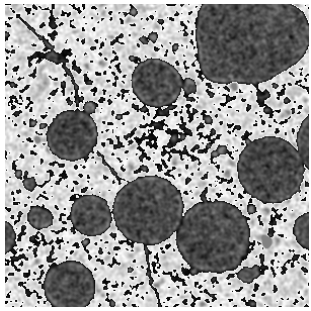

Figure 19.6: Microtomography image of sample Bul 61: enlargement around a crack.

19.3.2 Thermal conductivity

In this section, we consider the thermal conductivity problem for the lightweight concrete modeled by Fick's diffusion law. We consider the permanent regime only and neglect heat transfer due to convection. In theory these effects should be accounted for at 10°C. The thermal conductivity of retained air at 10°C is $\lambda_a \approx 0.0249$ W/m/K, whereas that in the cement paste is unknown. Using the scheme in (Willot, Abdallah, and Pellegrini 2014), we have carried out Fourier computations for varying values fo the local thermal conductivity $\lambda_c = 0.5$, 0.75 and 1 W/m/K in the cement paste. The effective thermal conductivity λ^{FFT} predicted by FFT are given in Tab. (19.3). These values are slightly lower than the Hashin-Shtrikman upper-bounds. Due to the high contrast of properties, we observe a linear relation $\lambda^{FFT} \approx b\lambda_c$ where b is a constant that depends on the microstructure. The choice $\lambda_c = 0.90$ and $\lambda_c = 0.75$ allows one to recover the experimental measurements for Bul 55 and Bul 61, respectively.

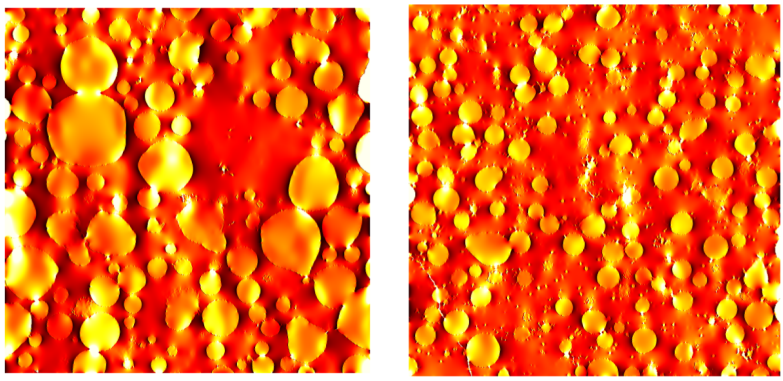

(a) Bul 55 (b) Bul 61

Figure 19.7: FFT maps of the temperature gradient $\partial_x T$ (with the x-axis oriented vertically on the map, top to bottom) in samples Bul 55 (a) and Bul 61 (b) with applied mean temperature gradient $\langle \partial_x T \rangle = 1$ (a.u.). Lowest and highest values in black and white, respectively.

Let us examine this difference assuming there exists micro-pores within the cement paste of Bul 61 at a much lower scales. In contrast with the elastic case, infinitesimaly-thin cracks should, in theory, have no effect on thermal properties, as long as the cracks are not insulating, so that micro-pores only should be considered. Assume again that the cement paste in sample Bul 55 is devoid of void and that the cement paste thermal conductivity in that case represents the conductivity of an undamaged cement paste $\lambda_u = 0.90$. The volume fraction of micro-pores within the cement paste is $f_m = 9\%$

	$\lambda_c = 0.5$	$\lambda_c = 0.75$	$\lambda_c = 1.0$
Bul 55	0.19	0.28	0.37
Bul 61	0.63	0.47	0.32

Table 19.3: Effective thermal conductivity of samples Bul 55 and Bul 61 for increasing values of the thermal conductivity λ_c (in W/m/K) in the cement paste, as predicted by numerical Fourier-based methods.

(i.e. 0.06/0.64) for sample Bul 61. We use the Hashin and Shtrikman upper bound to compute the thermal conductivity of the damaged cement paste λ_d, and obtain:

$$\lambda_d = \lambda_u + \left(\frac{1}{f_m} \frac{1}{\lambda_a - \lambda_u} + \frac{1 - f_m}{3 f_m \lambda_u} \right)^{-1} \approx 0.79 \quad (\mathrm{W/m/K}).$$

The above value, obtained by taking into account microporosity alone, is close to the value infered from FFT computations and experimental data. Indeed, as seen previously, a value of 0.75 W/m/K in the cement paste of sample Bul 61 allows one to recover the measured macroscopic conductivity. Although these considerations give a possible scenario for the thermal conductivity, its validity can only be confirmed by additional experimental measurements and images.

19.4 Conclusion

In this work, we have investigated the homogenized thermal and elastic properties of lightweight concrete, using Fourier numerical methods and standard homogenization theories. Two samples with different porosity have been considered. The results are as follow. Our study suggests the presence of micro-porosity and possibly micro-cracks in the cement paste of one of the two concrete samples, which contains the smallest pores. Experimental measurements for the effective elastic and thermal properties can be recovered for a Poisson ratio of 0.17, roughly, Young modulus of 51 GPa and thermal conductivity of 0.9 W/m/K in an *undamaged* cement paste. In the damaged cement paste, there exists a micro-porosity of 9% and a population of cracks with density about 0.2. Although the presence of cracks has been observed in the microtomography image of the damaged cement paste, experimental data is needed to confirm this scenario.

Acknowledgements The authors are grateful to CERIB for the financial support of A. Vannier-Moreau's internship at École des Mines, to Patrick Rougeau and François Jacquemot (CERIB) who provided concrete samples and experimental data, to Alain Fanget (CEA, Gramat) who performed the microtomography images and to Beatriz Marcotegui for useful suggestions on image segmentation.

References

Bristow, J. R. (1960). "Microcracks, and the static and dynamic elastic constants of annealed and heavily cold-worked metals". In: *British Journal of Applied Physics* 11.2, p. 81.

Kim, H. K., J. H. Jeon, and H. K. Lee (2012). "Workability, and mechanical, acoustic and thermal properties of lightweight aggregate concrete with a high volume of entrained air". In: *Construction and Building Materials* 29, pp. 193–200.

Michel, J.-C., H. Moulinec, and P. Suquet (2000). "A computational method based on Augmented Lagrangians and Fast Fourier Transforms for composites with high contrast". In: *Computer Modelling in Engineering & Sciences* 1.2, pp. 79–88.

Otsu, N. (1979). "A threshold selection method from gray-level histograms". In: *IEEE transactions on systems, man, and cybernetics* 9.1, pp. 62–66.

Willot, F., B. Abdallah, and Y.-P. Pellegrini (2014). "Fourier-based schemes with modified Green operator for computing the electrical response of heterogeneous media with accurate local fields." In: *International Journal of Numerical Methods in Engineering* 98, pp. 518–533.

Willot, F., H. Trumel, and D. Jeulin (2018). *The thermoelastic response of cracked polycrystals with hexagonal symmetry*. Submitted to Proceedings of the Royal Society A.